communications earth & environment

Article

A Nature Portfolio journal

https://doi.org/10.1038/s43247-026-03672-z

Arsenic-cycling metabolism recorded in hot spring silica deposits

Silvina Slagter[1,2] ✉, Kimberly Myers[1], Diego M. Guido[3], Bhoopesh Mishra[4], Thaïs Couasnon[1], Gernot Arp[5], Stefan V. Lalonde[6] & Mark A. van Zuilen[7]

Identifying early-life remnants is challenging due to the alteration of biosignatures over billions of years. Siliceous sinter deposits provide a unique window into the ancient biosphere due to their widespread occurrence in the ancient rock record and their excellent potential for preserving biosignatures. Indeed, hot spring silica deposits often preserve microbial traces, including microfossils, microbial mats, and stromatolites. In this study, we use synchrotron X-ray Absorption Near Edge Spectroscopy to investigate the distribution and speciation of Arsenic, a key element in microbial life, within organic matter-bearing silica sinters along an outflow channel of a modern hot spring in the Atacama Desert (El Tatio, Chile) and within organic matter-bearing, high-temperature facies of an extinct Jurassic geyser mound (Claudia, Argentina). We demonstrate that the coexistence of Arsenic(III) and Arsenic(V) is preserved within organic matter, and that the co-occurrence of Arsenic(III) and Arsenic(V) in hydrothermal sinter deposits can be used as an indicator of microbial activity in the fossil record. This finding serves as an additional tool in the search for fossil biosignatures in the early Earth rock record.

Microbially mediated textures within sedimentary deposits, especially those associated with redox-sensitive metal and metalloid enrichments, serve as excellent archives for examining the co-preservation of geochemical signatures and organic matter in ancient deposits[1–4]. High arsenic (As) concentrations associated with organic globules in 2.7-billion-year-old carbonate stromatolites from Western Australia, comparable to those in modern microbialites from Big Pond (Bahamas), have been proposed as biosignatures, representing metabolic pathways of early life[5,6]. Recent studies indicate that As concentrations were higher before the rise of atmospheric oxygen in marine environments and that As could be bound within microbial mats[7]. Modern examples in lacustrine environments demonstrate that As is complexed by hydrous ferric oxides[8,9] and sulfide minerals[7], but a significant proportion of As can also be processed by microorganisms, including the oxidation of As(III) (arsenite) to As(V) (arsenate) via anoxygenic photosynthesis, as well as the reduction of As(V) to As(III) during anaerobic respiration[6,10,11]. These examples include the hypersaline Mono Lake (California[10]), Searles Lake (California[12]), high-altitude Andean lakes such as Laguna Socompa[13], La Brava[14], and Diamante[15,16], as well as hypersaline lagoons such as those of Shark Bay[17]. In all cases, arsenic cycling is linked to lacustrine or lagoon deposits, and As-based phototrophy is often associated with carbonate and sulfide-rich environments[14] but has not yet been described in silica-rich deposits. Furthermore, whether the spatial association of mixed-valence As with organic matter can provide an additional indicator of microbial activity in the fossil record remains untested.

It has been recently shown that the mere presence of As enrichment does not necessarily result from microbial As-cycling metabolism, since dead organic material can also bind As[18]. This means that As enrichment in a microbial mat can be caused by hydrothermal circulation with high-As fluids. For instance, during diagenesis, As could be released by partial dissolution and oxidation of sulfides and subsequently accumulate in carbonaceous matter. In that case, however, the remnant microbial mat would adopt an As redox speciation similar to that of the circulating fluids. As speciation that deviates from that of the host rock, e.g., a remnant microbial mat containing both As(III) and As(V), could be an indication of As-cycling metabolisms[18].

Considerable amounts of As are found in siliceous hot spring microbial mats, which are analog environments of the conditions in which Precambrian microbial life evolved and thrived[19–21]. Examples include Champagne Pool, New Zealand[22], and outflow channels in the El Tatio Geyser Field, Chile, and Yellowstone National Park, USA[23–25]. Like many modern

[1]Institut de Physique du Globe de Paris, CNRS-UMR7514, Paris, France. [2]Instituto de Ciencias de la Ingeniería, Universidad de O'Higgins, Rancagua, Chile. [3]Instituto de Recursos Minerales (INREMI), CONICET and Facultad de Ciencias Naturales y Museo, Universidad Nacional de La Plata, La Plata, Argentina. [4]Physics Department, Illinois Institute of Technology, Chicago, IL, USA. [5]Geobiology Division, Geoscience Centre, Georg-August-Universität Göttingen, Göttingen, Germany. [6]UMR6538 Laboratoire Geo-Ocean (CNRS/UBO/IFREMER/UBS), European Institute for Marine Studies, Plouzané, France. [7]Naturalis Biodiversity Center, Leiden, The Netherlands. ✉e-mail: silvina.slagter@uoh.cl

hot springs, the Precambrian Earth's hydrothermal systems likely contained high concentrations of reduced As(III)[6]. Arsenic concentrations in silica sinter deposits associated with sulfides have been reported to reach values as high as 1000 mg kg^{-1} [26], with lower values observed in the Miocene Atastra Creek sinter, USA (15–972 mg kg^{-1} [27]) and the Late Miocene Whitianga Volcanic Centre, New Zealand (0.9–64 mg kg^{-1} [28]). Zones of As enrichment have also been found draping digitate microfabrics of sulfidized stromatolites in the 3.48 Ga Dresser Formation, though these were attributed to diagenesis[29,30].

These environments are, therefore, ideal for examining the preservation of various As-bound phases during the silicification process and assessing the potential to trace As-based metabolisms in the rock record. To test the utility of arsenic as a redox-sensitive metabolic tracer in ancient, silicified deposits and assess the impact of diagenetic overprint on these signatures within hydrothermal environments, here we compare a modern silicified microbial mat with a Jurassic-age silicified geyserite (a dense, finely laminated structure similar in appearance to microstromatolites[31]) that forms in high-temperature vent settings through repeated wetting and drying of surfaces by boiling/splashing fluids. We studied two localities: Geyser Asesino (GA) in the modern El Tatio Geyser Field in the Atacama Desert, Chile, and the Late Jurassic, well-preserved Claudia paleo-hydrothermal system sinter facies in Argentinean Patagonia. El Tatio hosts geothermal fluids with exceptionally high arsenic (As) concentrations (0.5 mM) and low iron (Fe) levels (10–20 µmol L^{-1}), presenting unique conditions for examining As speciation unrelated to iron sulfides[24,25], which typically inhibits photosynthetic As(III) oxidation[25]. Similarly, the Jurassic Claudia sinter exhibits elevated As concentrations not bound with Fe-rich phases[32].

Geological context

The El Tatio Geyser Field is the third-largest geyser field in the world, located in the Atacama Desert (Region II), Chile (Fig. 1). It is notable for its high altitude, high evaporation rates, low rainfall, and high ultraviolet flux[33–35]. Abundant digitate sinter forms in the shallow discharge channels (<40 °C[36]) of near-neutral alkali chloride hot springs such as Geyser Asesino (GA) (Fig. 2), with other thermal features including hot and boiling pools, mud pools, and fumaroles[33,37]. These discharge channels typically have shallow flowing waters, which support a diverse assemblage of microorganisms, with the most abundant being cyanobacteria and diatoms associated with thin, green microbial mats[37]. X-ray diffraction and petrography of the modern sinter samples used in this study indicate that they are predominantly composed of opal-A, suggesting minimal diagenetic modification[32,34].

The Late Jurassic Claudia paleo-hydrothermal system, located in the Deseado Massif, Argentina, is characterized by travertine and silica sinter deposits[38]. One of its best-preserved sinter facies is the Loma Alta outcrop, located in an ENE trend parallel to the Seco River and interbedded with volcanic and sedimentary units. Three main sinter facies are recognized in the Loma Alta hot spring deposit: high-temperature, mid- to low-temperature sinter, and a late hydrothermal breccia. The high-temperature sinters are represented by columnar geyserite fabrics (Supplementary Fig. 1)[30] and characterized by abundant kerogen relative to lower-temperature facies[39,40].

Results

El Tatio (modern site)

Observations of the GA channel site show regular water discharge as a short-cycle (~5 min) eruption at the local boiling point (86 °C)[41]. In the GA channel, water exits in a 0.7-m-wide boiling source pool, walled by a shallow (4–6 cm high) sinter rim that experiences occasional overflow during the highest surge oscillations and highest wind velocities (Fig. 2). Temperature oscillations are represented in Supplementary Fig. 2. The pH is near neutral along the channel (Supplementary Table 1), and aqueous As variations are depicted in Supplementary Fig. 3.

The mat–sinter-associated sample taken from the GA channel is composed of an amorphous silica (opal-A) matrix (Fig. 3)[32–36]. Thin laminations of microbial mat (0.5 mm) are observed on the lower faces of the sinter, intercalated with growth edges. Bacterial filaments are aligned in tightly packed, vertical pillars characteristic of palisade fabric oriented normally to the growth surface, as revealed by CLSM (Fig. 3). DNA amplicon 16S results are reported in Supplementary Fig. 4.

Submillimeter-thick layers exhibiting enrichments in As were identified in El Tatio samples, and As was not observed to be associated with Fe (Fig. 4). Three microfacies display contrasting geochemical behavior: a high-temperature digitate sinter formed by evaporation (area 1), a finely laminated sinter (area 2), and a subaerial microbial mat (area 3). The organic matter in area 3 commonly forms thin laminations parallel to silica fabrics. Stacked FTIR spectra along the transect from area 3 to area 2 show the progressive development of the characteristic Si–O–Si stretching band (~1000–1200 cm^{-1}). Within area 3, the mat exhibits strong fluorescence emission, clearly distinguishable from the sinter (Supplementary Fig. 5). Both the digitate sinter and the laminated sinter contain variable amounts of As and Fe, whereas the underlying microbial mat (area 3) contains uniformly high As and low Fe concentrations. Reduced As species (As(III)) were detected by XANES associated with organic matter (Fig. 5). Similarly, sulfur XANES spectra document a transition from reduced S species at the base of the mat to more oxidized sulfur in the upper sinter layers. These coupled As–S redox gradients across a very thin (~0.5 mm) interval. Reduced As(III) species were also detected in the boundary of the sinter, while the silica sinter itself contained more As(V) (Fig. 5). Subaerial mat communities over high-temperature water are dominated by *Chloroflexus* sp. (Supplementary Fig. 4).

Claudia (Jurassic site)

The Claudia geyserite sinter facies is characterized by quartz and contains locally elevated As concentrations[32]. Arsenic is not bound to Fe and is

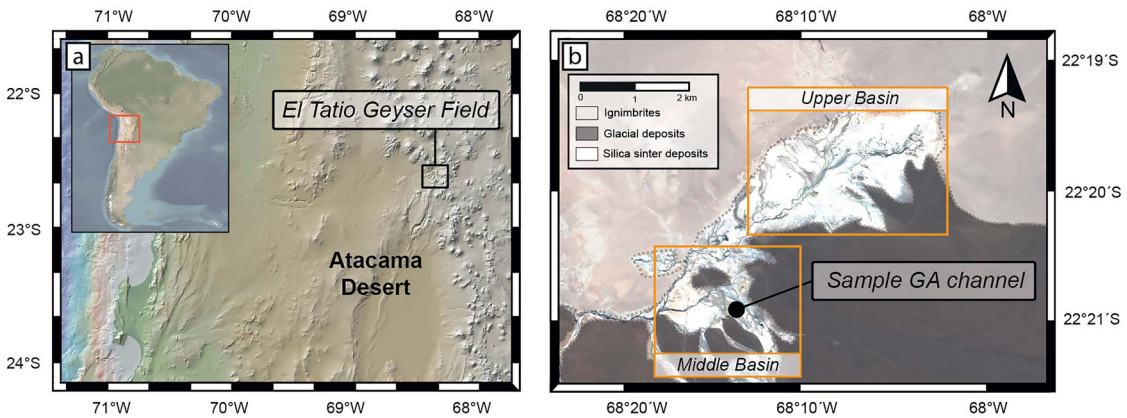

Fig. 1 | El Tatio samples location. (**a**) Location of El Tatio, Chile, at 4300 m elevation. The inset shows the location area in South America. (**b**) Distribution of geothermal features across the El Tatio basin, showing modern geyser deposits (Middle Basin) and the GA channel where µXRF/XAS was performed. Modified from Slagter et al.[34].

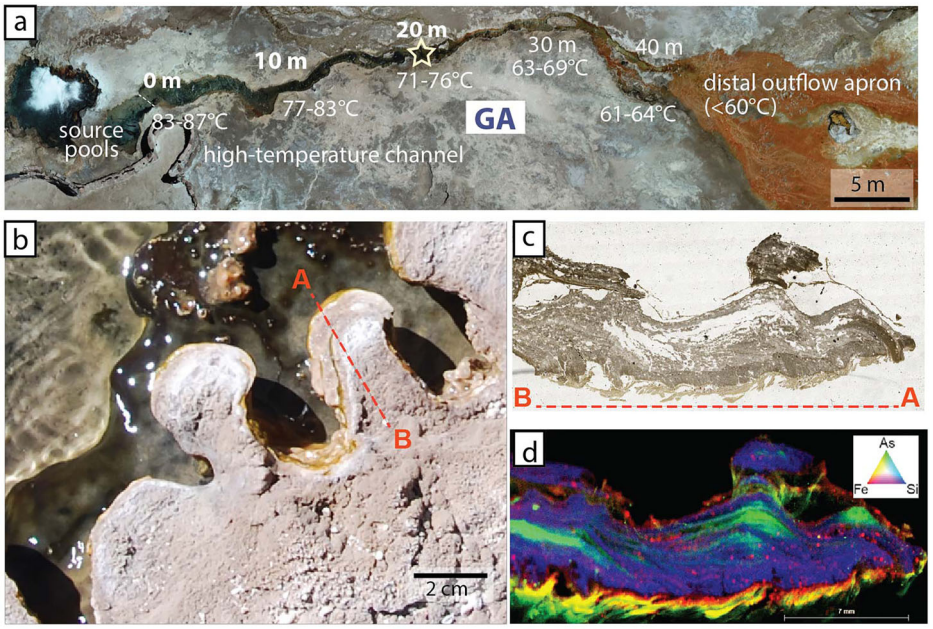

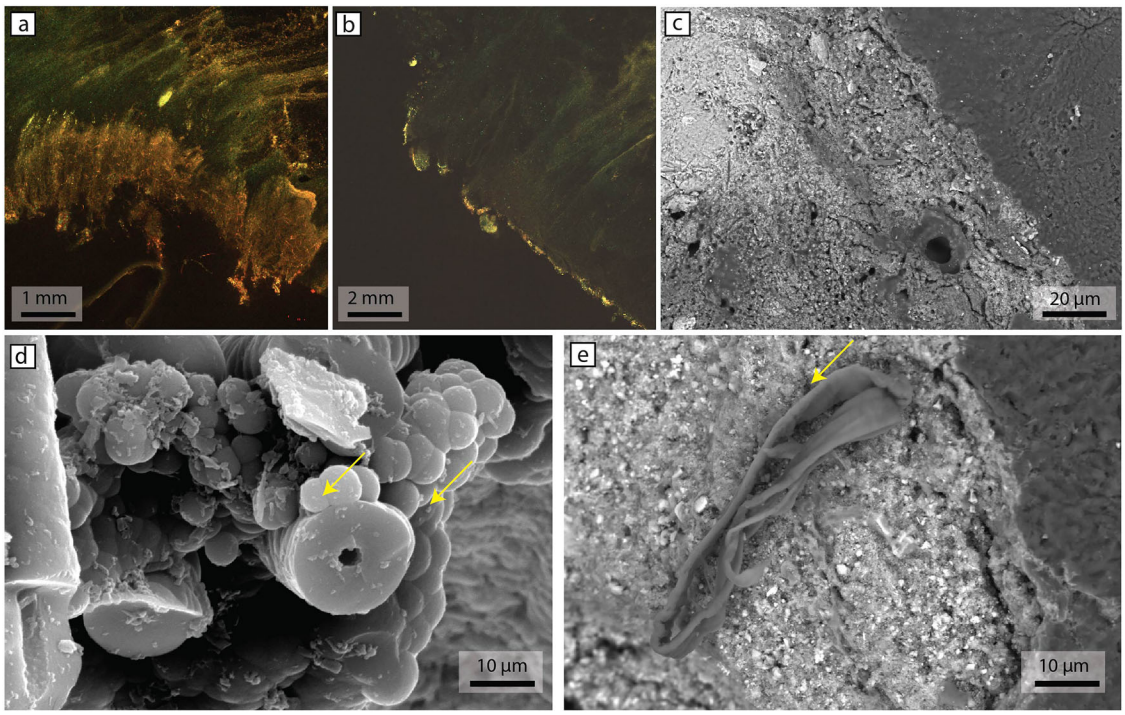

Fig. 3 | El Tatio GA channel microbes preserved in sinter. a, b CLSM images showing the tightly packed, vertical pillars characteristic of palisade fabric oriented perpendicular to the growth surface, and **c–e** SEM images showing the sheath of bacteria entombed in silica (opal-A), highlighted by arrows.

present as As(III) in globules (possibly organic-bound) and As(V) in silica associated with the geyserites. The XANES spectra collected in the globule regions show a higher contribution of As(III) than As(V) (Fig. 6). In contrast, the sinter matrix is associated with As(V). As was not observed to be associated with Fe (Supplementary Fig. 6).

Discussion and conclusions

The El Tatio samples investigated here exhibit a typical laminated structure composed of opal-A, forming millimeter- to centimeter-scale knobs (Supplementary Fig. 7). We identified a submillimeter-thick band exhibiting significant As enrichments. In this enriched interval, organic matter occurs as diffuse strands and filamentous aggregates that define a discontinuous network, consistent with the preservation of organic-rich microbial material incorporated during early silica precipitation (Supplementary Fig. 5). While features attributable to the microbial material (e.g., adsorption by aliphatic and aromatic compounds at ~2925–2960 cm^{-1} and ~1500 cm^{-1}, respectively) were not observed in FTIR spectra, likely due to their low concentrations and potential overlap with strong silica adsorption features, epifluorescence imaging reveals fluorescence signals that are sharply localized within the microbial mat, particularly near its upper boundary, consistent with the presence of cyanobacterial carotenoids (fluorescence between 500 and 600 nm)

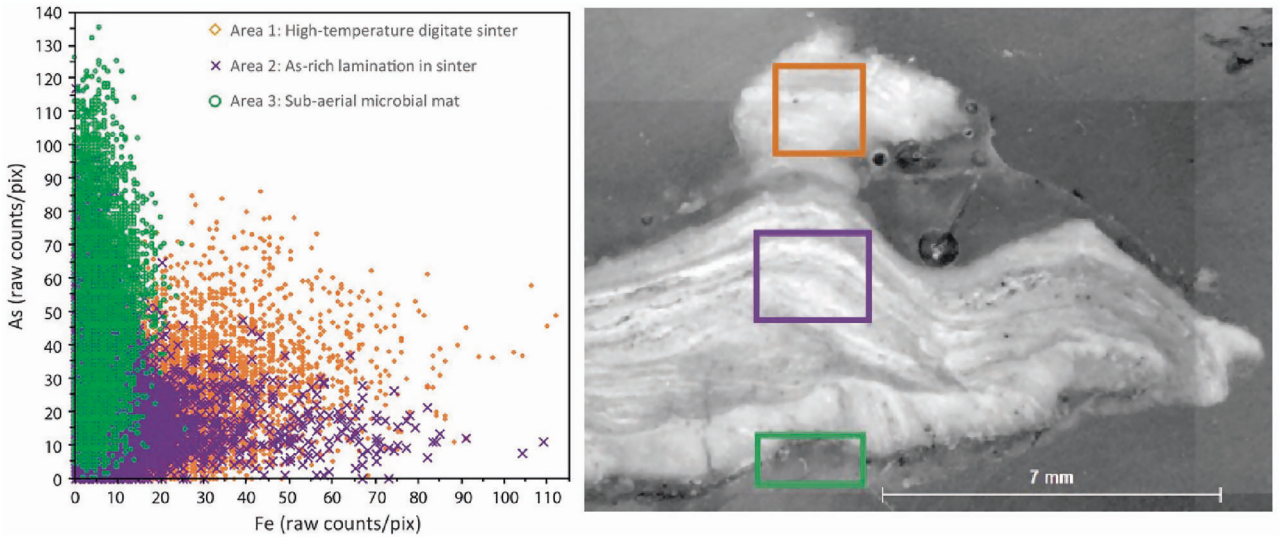

Fig. 4 | Synchrotron μ-X-ray fluorescence (μXRF) mapping of As and Fe. The relationship between Fe and As was compared in three areas of the El Tatio GA channel: (1) digitate sinter formed by evaporation (orange), (2) laminated sinter (purple), and (3) microbial mat (green). Areas (1) and (2) contain significant As not associated with Fe, bound in organics, or to non-Fe mineral phases. The area of focus for this study is the interface between sinter and microbial mat (green box), to compare to the preservation of As in sinter formed by morphologies of sinter laminations (purple and orange boxes). Area 1: $R^2 = 0.55$; area 2: $R^2 = 0.26$; area 3: $R^2 = 0.85$.

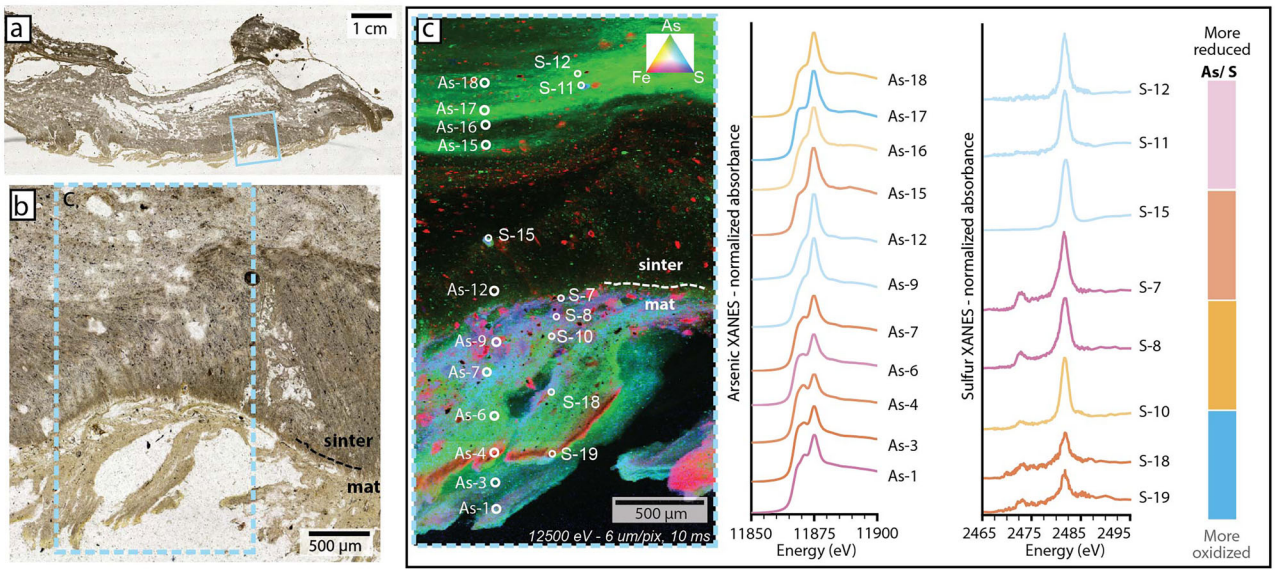

Fig. 5 | XANES results from El Tatio. (**a**) Photomicrograph showing the sampled transect A–B in Fig. 2. (**b**) Mat–sinter interface showing the area where μXANES analyses were performed. (**c**) μXRF map and associated μXANES spectra of As and S across the microbial mat–sinter interface. Colors in the μXRF map denote the distribution of Fe, As, and S. The spectra show peaks near 11,867 and 11,875 eV, corresponding to As(III) and As(V), respectively, with reduced As(III) predominating in microbial mats and oxidized As(V) enriched in the sinter. Autofluorescent compounds associated with cyanobacterial carotenoids (fluorescence between 500 and 600 nm) are shown in Supplementary Fig. 5.

(Supplementary Fig. 5)[42]. More concentrated As bands are observed in the mat compared to the sinter (Fig. 2). Importantly, when plotting against Fe, As shows no consistent spatial correlation, suggesting that its accumulation is not governed by coprecipitation with iron (Fig. 4). μXANES spectra of As and S across the microbial mat–sinter interface revealed that reduced As is associated with the mat, whereas oxidized species dominate the sinter (Fig. 5). These findings align with models in which arsenic is incorporated into microbial communities through anoxygenic phototrophy, detoxification, or chemolithoautotrophy[5,6,43,44]. Given the analytical limitations for directly detecting organic carbon using XRF, we interpret these results as evidence of a spatial association consistent with possible As–organic interactions.

In the Jurassic Claudia samples, micrometer-scale carbonaceous globules show enrichment in As unaccompanied by Fe (Fig. 6 and Supplementary Fig. 6). Other trace metals such as Cu, Ti, and Zn, whose origin is debated, show a lack of co-localization between these elements and arsenic, further supporting this interpretation (Supplementary Fig. 8). The clotted organic matter found in Jurassic sinter closely resembles reworked remains of microorganisms as described in the Barberton Greenstone Belt, which origin is debated as either chemotrophic or phototrophic[45]. Furthermore,

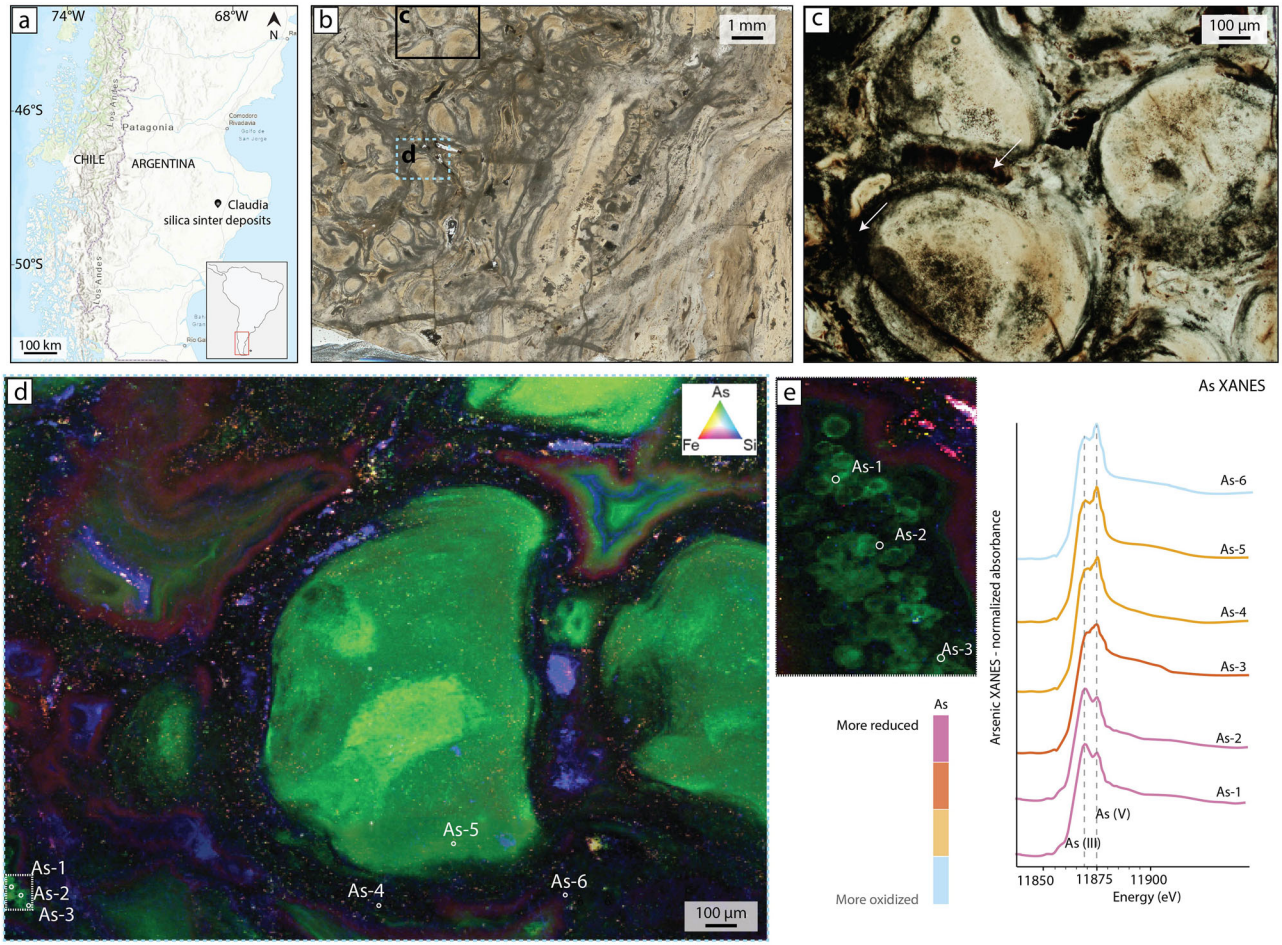

Fig. 6 | Results from Claudia Jurassic sinter. (**a**) Simplified shaded relief map of southern Patagonia showing the location of the Late Jurassic Claudia paleo-hydrothermal system. Inset: regional context within South America. Modified from Guido et al.[38] (**b**) Transmitted light micrograph of a cross-section through geyserite facies displaying a clotted carbonaceous texture. (**c**) Magnified view of the area in **b**, highlighting organic-rich clotted textures associated with the geyserite; white arrows indicate organic matter. (**d**) XRF elemental map showing arsenic (As) concentrations in green. Arsenic occurs independently of iron (Fe) and is present as As(III), near 11,867 eV in globular features within the organic-rich zones, and As(V), 11,875 eV surrounding the geyserite structures, indicated by XANES spectra. (**e**) Magnified area showing clotted organic matter at points As-1, As-2, and As-3, morphologically similar to carbonaceous textures reported in the Archean Josefsdal cherts, interpreted as remains of chemotrophic organisms and analogs to microfossils.

these silicified carbonaceous structures described from the ~3.3 Ga Josefsdal Archean chert exhibit arsenic accumulation[46] and have been interpreted as possibly linked to microbial As metabolism[3]. There, sulfide minerals often co-occur with the carbonaceous clots and may represent either sources of the detected As signal or substrates for As mobilization into the carbonaceous particles. In the Jurassic Claudia samples, arsenic is predominantly present as As(III) with no or only minor amounts of other trace metals, while As(V) is more strongly enriched in the surrounding silica sinter (Fig. 6). This argues against post-depositional incorporation of As by organic matter and instead supports a biologically mediated origin linked to microbial As cycling. The enrichment of arsenic could be associated with extracellular polymeric substances (EPS)-rich textures and microbial cells, likely reflecting biologically mediated accumulation[5]. Alternatively, the organisms may be producing As(III) locally in the mat, allowing As to be incorporated into the silica that nucleates around the EPS. The preservation of reduced As species in the Jurassic sinter emphasizes the long-term stability of microbial arsenic signatures through silica diagenesis (from amorphous phases to quartz). This suggests a persistence of microbial arsenic-cycling signatures through deep time (cf.[47]).

Multiple mechanisms can contribute to arsenic enrichment in sinters[48]. At El Tatio, total dissolved arsenic behaves conservatively along discharge channels, with concentrations increasing with distance along discharge channels in proportion to chloride due to evaporative concentration (Supplementary Fig. 3)[9]. Arsenic, as a chemical analog of phosphate and glycerol, is readily taken up by cells through both low- and high-affinity Ars-B and Ars-C transport systems, primarily as a detoxification mechanism[49]. The low concentrations of carbonate and phosphate in the waters at El Tatio reduce potential competitive inhibition of arsenic sorption[9]. Exposure of sinter to continuous or episodic inundation by silica-saturated hydrothermal fluids promotes the development of negatively charged surfaces via siloxane bridging[50], which significantly inhibits As(III) sorption under the slightly alkaline conditions typical of the channels[51]. In contrast, As(V) sorption is markedly reduced only at pH values exceeding 7 (at 25 °C), a condition that may occur progressively downstream as pH increases and As(III) is oxidized[9]. Moreover, given the lower solubility of arsenate relative to arsenite, enzymatic oxidation of As(III) to As(V) may facilitate its incorporation into organic matrices. Accordingly, the presence of arsenic in its reduced form (As(III)) within these deposits—despite physicochemical conditions that favor the oxidation and sorption of As(V)— suggests a biologically mediated origin, as purely inorganic processes would be expected to favor the predominance of As(V) in oxidized surface environments.

At El Tatio, aerobic arsenite oxidizers such as *Chloroflexus* sp. and various Proteobacteria enzymatically oxidize As(III), which subsequently accumulates as As(V) in biofilms that become rapidly silicified during evaporation[25]. Anoxygenic phototrophs, including *Chloroflexus* sp., and

purple sulfur bacteria, such as *Ectothiorhodospira* sp., also utilize arsenite as an electron donor[52]. The presence of arsenite oxidation genes in these microorganisms supports their role in arsenic cycling within microbial mats[15]. In addition, the presence of anaerobic As(V)-respiring organisms—including chemolithoautotrophic and chemoorganoheterotrophic microorganisms—suggests that arsenic metabolism spans a wide range of ecological niches and metabolic pathways[53]. DNA amplicon libraries from subaerial mats in the GA stream transect also display a high abundance of S-cycling microorganisms, including *Thiobacillus* sp. (Supplementary Fig. 4), despite low aqueous concentrations of reduced sulfur species, Fe(II), and dissolved inorganic carbon (DIC), where temperatures decrease to allow mats to propagate[9,25]. El Tatio's high elevation results in low oxygen saturation, limiting aerobic metabolisms such as methanotrophy and nitrification–denitrification[14]. Although these pathways are rare in modern ecosystems, phylogenetic and geochemical evidence suggests that arsenotrophic metabolisms played a central role in early Earth energy metabolism[10,54].

Experimental data show that arsenate reduction is energetically favorable even in sulfide-poor, high-temperature settings, such as those observed at the El Tatio Geyser Field[14]. In silica-rich environments, such as El Tatio, rapid entombment of microbial mats could lead to exceptional preservation of both organic matter and As redox speciation (Fig. 5). Previous studies in lacustrine and marine carbonatic environments have highlighted the role of rapid mineral precipitation in the preservation of As-rich globules[5,6]. This enrichment has been attributed to the binding capacity of microbial EPS[18]. The ability of organic matter to bind As has been proposed to explain its accumulation in both modern and ancient environments based on observations of microbialites from Big Pond (Bahamas) and 2.7-billion-year-old stromatolites from the Tumbiana Formation, Western Australia[5,6]. In both examples, As is embedded in carbonate matrices and unassociated with sulfides or other metals, suggesting a primary microbial origin[5,6]. In the modern example from Bahamas, the changes in the elemental distribution patterns through early diagenesis were traced from the centimeter to the micrometer scale, showing the potential of this element to be interpreted as a biosignature in the modern system as well as in the rock record[6]. This observation aligns with recent findings from hydrothermal vent systems, where arsenic filaments have been linked to microbial activity[55]. While most published examples of arsenic preservation in the rock record come from carbonate deposits[5,6], the extremely low DIC (~0.5 mM DIC) at El Tatio is sufficiently low to prohibit carbonate precipitation with cooling along channel outflows[9]. This lends further support to the critical enzymatic role of arsenic bioaccumulation and redox transformation in El Tatio silica sinter, demonstrating that As preservation is coupled most closely to organic carbon deposits. Moreover, arsenic methylation and excretion, processes thought to have originated during the Archaean Eon, point to a deep evolutionary history of microbial arsenic metabolism[56]. This incorporation of arsenic into organic matrices through anoxygenic phototrophy or chemolithoautotrophy performed in the GA channel by abundant organisms such as *Chloroflexus* sp. (Supplementary Fig. 4) offers critical insights into the interaction between microbial life and arsenic in natural systems[43]. The preservation of reduced As species in As(V)-dominated Jurassic sinters highlights the persistence of microbial arsenic metabolism throughout diagenesis. This persistence implies that arsenic redox patterns and distributions may serve as a durable biosignature in other silica-rich deposits beyond the specific hydrothermal setting investigated here. Extending this framework to older hydrothermal systems, including Archean examples, such as the one found in the 3.5 Ga Dresser Formation, Pilbara, Western Australia, could clarify the extent to which such signatures are preserved over geological timescales[57]. Similar biosignatures would be expected in a range of depositional environments. Shallow-marine Proterozoic cherts—where phototrophs and chemolithotrophs are known to have thrived—provide favorable conditions for the development and preservation of these signals. Likewise, lacustrine silica deposits and deep-sea hydrothermal vents, both of which host active arsenic-based metabolisms today, represent environments where comparable redox patterns could have developed and been preserved. These considerations extend naturally to astrobiology. Silica-rich hydrothermal settings on early Mars, where redox-active elements and steep thermal gradients occur, are plausible analog environments in which arsenic-based metabolisms could have been energetically sustained[31,58]. Thus, the As redox distributions documented here highlight a broader framework for tracing microbial activity across both Earth's deep-time sedimentary record and potentially habitable planetary settings.

In conclusion, our findings highlight the critical role of microbial life in arsenic cycling within silica-rich environments. The incorporation of arsenic into microbial mats, particularly within EPS, and its subsequent preservation through silica precipitation, offers a plausible mechanism for the long-term stability of arsenic-bearing biosignatures. The preservation of reduced arsenic in modern and Jurassic silica-rich environments suggests that arsenic microbial textures can be preserved throughout silica diagenesis, providing a potential biosignature for ancient life. These insights enhance our understanding of arsenic's role in early life on Earth and also suggest that similar processes could be at play in other silica-rich planetary environments, making arsenic a potential target for astrobiological exploration.

Methods

El Tatio sample collection

Subaerial sinter and associated microbial mats were collected in 2018 from the high-temperature zone of the outflow channel of the Geyser Asesino (GA) in the Middle Basin of El Tatio, Chile (Fig. 2). The temperature of the channel was monitored through time, and samples were taken from ~20 m from the source. Samples were frozen on-site and upon return, were dehumidified under a laminar flow hood and quickly embedded in epoxy resin, in order to prevent shrinking and desiccation of microbial mat, which could alter the contacting surface between sinter and biofilm, and to limit exposure to air. Several cycles of vacuum pumping were performed to remove air from the epoxy resin during hardening. Small slices (20–40 mm^2) were cut using a 50/50 filter-sterilized water and EtOH solution. Major and trace element concentrations in the aqueous and solid phases were measured upon return to the laboratory.

Claudia samples collection

Within the Jurassic (~150 Ma) age Deseado Massif of Argentine Patagonia, numerous paleo-hot spring deposits have been discovered[59]. Geyserite sinter facies from the Claudia locality (Loma Alta outcrop)[38] are analyzed here (sample C127) to compare the preservation potential of biosignatures from fossilized microbial filaments with that of the El Tatio modern samples.

Major and trace element analysis

Three samples of each locality were measured for major and trace elements, including Si, B, Na, Cl, dissolved inorganic carbon (DIC), total dissolved arsenic (AsT), and Fe, were analyzed at the Institut Universitaire Européen de la Mer (IUEM, Brest, France). All preparation for solution-mode ICP-MS and ICP-OES analyses was conducted in a class 1000 clean laboratory. Analyses were performed using a Horiba Yvon Ultima 2 ICP-OES at the Pôle Spectrométrie Océan (PSO), IUEM. Calibration was performed using eight international geostandards (CB, BELC, JB, BEN, ACE, WSE, ME, and GSN), with reference values from ref.[60]. Pure quartz was used as a high-SiO_2 standard. Dissolved arsenic speciation was determined following a field-separation and ICP-MS approach adapted from ref.[61].

For trace element analysis, prior to analysis, samples were diluted to 5 mL with 2% HNO_3, and 1.5 mL was archived. Trace elements were analyzed using a Thermo Element2 HR-ICP-MS at PSO. Calibration was based on gravimetrically prepared multi-element standards (0.5, 5, and 50 ng g^{-1}), measured periodically throughout the session. A 5 ng g^{-1} indium (In) spike was added to all samples, standards, and rinses to monitor signal stability and correct for instrumental drift. Each sample and standard was bracketed with a rinse, from which data were used to determine detection limits. Precision was monitored by including

international standards IF-G, BCR-2, and BHVO-2, prepared in duplicate and treated as unknowns.

Confocal laser scanning microscopy

Field sinter samples for confocal laser scanning microscopy (CLSM) were fixed immediately after collection using a modified protocol based on previous work[62]. Samples were immersed for 3 h in freshly prepared 4% paraformaldehyde buffered with phosphate-buffered saline (PBS; pH 7.2; 10 mM sodium phosphate, 130 mM NaCl), then rinsed twice with PBS and stored at 4°C. Samples were dehydrated through a stepwise ethanol series (15%, 30%, 50%, 70%, 90%, 99%, and 99%; 1 h per step) and stained en bloc with Sytox Green (Thermo Fisher Scientific S7020; 1:5000 dilution in 50% EtOH/PBS). Two representative samples were embedded in LR White resin (medium grade, London Resin Company Ltd.) following the manufacturer's recommendations. Embedded samples were sectioned using a Leica SP1600 saw microtome to ~500 µm thickness, mounted onto glass slides with Araldite 2020 epoxy resin (Huntsman Advanced Materials Europe), and polished to a final thickness of ~50 µm. One section from each sample was subsequently treated with 10% KOH and stained for 10 min in the dark with Calcofluor White solution (Fluka 18909-100ML-F), rinsed with PBS, and sealed beneath a coverslip. Sytox Green fluorescence was used to visualize nucleic acids, whereas Calcofluor White was employed to detect extracellular polymeric substances (EPS), owing to its affinity for polysaccharides containing contiguous β-(1→4)-D-glucopyranosyl groups. Imaging was performed at the Geobiology Group, Geoscience Centre, University of Göttingen, using a Zeiss LSM 510 Meta NLO confocal microscope coupled to an Axiovert 200M microscope. Observations were conducted with water-immersion objectives at 40× and 63× magnification. Excitation was provided by Ar and HeNe lasers operating at 488, 543, and 633 nm, with emission collected at 500–530, 565–615, and 640–700 nm. The green channel captured nonspecific autofluorescence alongside Sytox Green emission; the yellow channel recorded nonspecific autofluorescence; and the red channel detected autofluorescence, including potential photopigment-related signals such as chlorophyll. Because detector amplification enhances weak emissions, all fluorochromes and pigments contributed to multiple channels to varying degrees. Spectral fingerprinting and linear unmixing were conducted using a 32-channel Meta detector and associated Carl Zeiss software. Calcofluor White fluorescence was additionally imaged using a femtosecond-pulsed Titan-Sapphire laser (Chameleon XR, Coherent) at 720 nm excitation with emission collected between 435 and 485 nm.

µ-X-ray fluorescence

Synchrotron µ-X-ray fluorescence (µXRF) mapping was conducted at the GSECARS 13-ID-E beamline, Advanced Photon Source (APS), Argonne National Laboratory, IL, USA. Samples consisted of a polished mount. These sections were carefully hand-polished on the cut face using 600 then 800 grit silicon carbide polishing paper (Buehler). This sample preparation technique was employed to avoid the use of glass slides. Maps were performed in a 24 mm^2 zone from the geyserite facies of the Loma Alta outcrop (Claudia paleo-hydrothermal system) and in samples from El Tatio modern channels to investigate the micrometer-scale distribution of As valence state across the As-rich zones. We used µ-XRF/XAS to determine the speciation, coordination, and preservation of As in subaerial sinter in two exceptionally preserved sinter deposits from modern and Jurassic age. Dwell times of the beam on each pixel were set to vary between 1 and 10 ms, and the beam size was 3 µm. Calculated attenuation lengths vary from ~13 to ~700 µm in SiO_2 (2.2 g cm^{-3}, at a 90°-beam incidence angle[63]).

X-ray absorption near edge structure (XANES) spectroscopy

In situ arsenic XANES spectroscopy measurements at the As K-edge were conducted at the GSECARS 13-ID-E beamline, Advanced Photon Source (APS), Argonne National Laboratory, IL, USA. The beamline can cover an energy range of 2.4–28 keV and uses a high-flux beam (≥4.5 × 1010 photons s^{-1}100 mA^{-1} mm^{-2}) that produces a high spatial resolution micro-focused 2 × 2 µm (µ-XANES) beam by using Kirkpatrick–Baez (KB) focusing mirrors. The energy of the Si (111) channel-cut monochromator was calibrated to the 11.8745 (±0.2) keV white line of the spectrum for clear double-sided adhesive tape. Spectra were collected at ambient temperature and pressure and covered a range of energy from 12,500 eV, with a step size of 0.1–0.3 eV at the As K-edge (11,820–12,000 eV) and 1 eV for the pre- and post-edge regions (0.5–3 s scan durations per energy step). Four different mineral standards were used for calibrating the XANES analysis of arsenic. These include: arsenopyrite (FeAsS), orpiment (As_2S_3), schneiderhöhnite, and scorodite[64]. Energies for S standards were mapped at 2470 eV (sulfides), 2474 eV (organic reduced groups, e.g., sulfhydryl), and 2481 eV (sulfate). These were used to fit the normalized spectra with the linear combination fitting method in the Athena software[65].

Petrography

Petrographic observations were carried out on the polished mounts using light microscopy, which also provided the foundation for the micro-scale geochemical analyses. Textures of interest were identified for X-ray fluorescence. Images were captured using an Olympus DSX1000 Digital Microscope, employing both bright-field and polarized reflected-light observational modes.

Scanning electron microscopy (SEM)

Before imaging, samples were rinsed with deionized water and air-dried before being placed directly on aluminum stages with carbon glue and sputter-coated with gold. SEM was performed at the Institut de Physique du Globe de Paris (IPGP) PARI analytical platform with a Zeiss Gemini SEM 500, FEG-SEM at 3–6 keV and a working distance of 5 mm. EDX spectra and maps were obtained separately using a Zeiss EVO MA-10 at 15 kV and a working distance of 12 mm.

Fourier-transform infrared (FTIR) spectroscopy

Reflectance FTIR spectroscopy was performed at the European Institute for Marine Studies, Plouzané, France. Spectra were acquired using a Jasco IRT-5200 infrared microscope coupled to a Jasco FT/IR-4600 spectrometer operating in reflected-light mode. Background spectra were collected on the metal sample holder prior to analysis. Reflectance spectra were recorded over the range 700–4000 cm^{-1} with a spectral resolution of 1 cm^{-1} using an aperture of 100 × 100 µm. Measurements were acquired along an approximately 6 mm transect across the sample in 300 µm increments, spanning epoxy, microbial mat, and sinter domains. Each spectrum was acquired for 10 s per point.

Epifluorescence imaging

Epifluorescence imaging was performed with a Zeiss binocular microscope equipped with an LED fluorescence source and a monochrome camera using Zeiss FL Filter set #38 (excitation 470 nm/emission 525 nm) at the Laboratoire de Planétologie et Géosciences, Angers, France. Five images were taken in reflected light and five using epifluorescence, and each was stacked using the mean stack feature of Adobe Photoshop to produce single grayscale images. The epifluorescence image was assigned to the R channel and the reflected-light image to the G and B channels, to create an RGB image. No further image processing or subjective enhancement was applied.

DNA sampling and analysis

Samples from the GA channel were immediately placed in sterile bags and stored between 0 °C and 4 °C in thermal insulating bags until they reached the laboratory. Within 1 week of sampling, the samples were frozen at −20 °C to preserve the DNA. Genomic DNA was extracted using a Qiagen™ DNeasy® PowerLyzer® PowerSoil® Kit (Qiagen Sciences, Germantown, MD, USA) following the manufacturer's protocols. The V4–V5 region of the 16S rRNA gene (515F–926R)[66] was sequenced to a depth of ~100k reads/sample on an Illumina MiSeq (Illumina Inc., San Diego, CA, USA) platform (MrDNA Labs, Shallowater, TX, USA) using bacterial tag-encoded FLX amplicon (bTEFAP®) sequencing technology[67]. Following standard quality control removal steps[68], filtered,

quality-, and chimera-checked 16S amplicon libraries containing an average of 70k reads/sample were aligned to cultured, database-accessioned environmental clones using the most recent Greengenes (v. 13.8) alignment database[69]. Generic- and species-level taxonomic assignments were made at the 97% and 99% cutoff levels, respectively. Resulting quality- and chimera-checked 16S amplicon libraries contained an average of 70k reads per sample.

Data availability

The authors declare that the data supporting the findings of this study are available in the data repository 10.5281/zenodo.20160239 and the manuscript supplementary information files.

Received: 7 September 2025; Accepted: 14 May 2026;
Published online: 22 May 2026

References

1. Poulton, S. & Canfield, D. E. Ferruginous conditions: a dominant feature of the ocean through Earth's history. *Elements* **7**, 107–112 (2011).
2. Huerta-Diaz, M. A. et al. Millimeter-scale resolution of trace metal distributions in microbial mats from a hypersaline environment in Baja California, Mexico. *Geobiology*, **10**, 531–547 (2012).
3. Hickman-Lewis, K. et al. Metallomics in deep time and the influence of ocean chemistry on the metabolic landscapes of Earth's earliest ecosystems. *Sci. Rep*. **10**, 4965 (2020).
4. Gangidine, A. et al. Trace element concentrations in hydrothermal silica deposits as a potential biosignature. *Astrobiology* **20**, 525–536 (2020).
5. Sforna, M. C. et al. Evidence for arsenic metabolism and cycling by microorganisms 2.7 billion years ago. *Nat. Geosci.* **7**, 811–815 (2014).
6. Sforna, M. C. et al. Patterns of metal distribution in hypersaline microbialites during early diagenesis: implications for the fossil record. *Geobiology* **15**, 259–279 (2017).
7. Chi Fru, E. et al. The rise of oxygen-driven arsenic cycling at ca. 2.48 Ga. *Geology* **47**, 243–246 (2019).
8. Inskeep, W. P. et al. Biomineralization of As(V)-hydrous ferric oxyhydroxide in microbial mats of an acid-sulfate-chloride geothermal spring, Yellowstone National Park. *Geochim. Cosmochim. Acta* **68**, 3141–3155 (2003).
9. Landrum, J. T. et al. Partitioning geochemistry of arsenic and antimony, El Tatio Geyser Field, Chile. *Appl. Geochem.* **24**, 664–676 (2009).
10. Oremland, R. S., Stolz, J. F. & Hollibaugh, J. T. The microbial arsenic cycle in Mono Lake, California. *FEMS Microbiol. Ecol.* **48**, 15–27 (2004).
11. Bia, G. et al. Arsenic in natural carbonates: the role of the biogeochemical conditions in its solid speciation. *Chem. Geol.* **583**, 120477 (2021).
12. Kulp, T. R. et al. Arsenic(III) fuels anoxygenic photosynthesis in hot springs biofilms from Mono Lake, California. *Science* **321**, 967–970 (2008).
13. Farías, M. E. et al. The discovery of stromatolites developing at 3570 m above sea level in a high-altitude volcanic lake Socompa, Argentinean Andes. *PLoS One* **8**, e53497 (2013).
14. Visscher, P. T. et al. Modern arsenotrophic microbial mats provide an analogue for life in the anoxic Archean. *Commun. Earth Environ.* **1**, 24 (2020).
15. Sancho-Tomás, M. et al. Geochemical evidence for arsenic cycling in living microbialites of a high altitude Andean lake (Laguna Diamante, Argentina). *Chem. Geol.* **549**, 119681 (2020).
16. Saona Acuña, L. A., et al., in Microbial Ecosystems in Central Andes Extreme Environments (eds. María Eugenia Farías & Diego Contreras), 275–284 (Springer, 2020).
17. Gudhka, R. K., Neilan, B. A. & Burns, B. P. Adaptation, ecology, and evolution of the halophilic stromatolite archaeon *Halococcus hamelinensis* inferred through genome analyses. *Archaea* **2015**, 241608 (2015).
18. Madrigal-Trejo, D., Baldes, M. J., Tamura, N., Klepac-Ceraj, V. & Bosak, T. Arsenic accumulation in microbial biomass and the interpretation of signals of early arsenic-based metabolisms. *Geobiology* **23**, e70024 (2025).
19. Konhauser, K. O., Jones, B., Reysenbach, A.-L. & Renaut, R. W. Hot spring sinters: keys to understanding Earth's earliest life forms. *Can. J. Earth Sci.* **40**, 1713–1724 (2003).
20. Tice, M. M. & Lowe, D. R. Photosynthetic microbial mats in the 3,416-Myr-old ocean. *Nature* **431**, 549 (2004).
21. Chaves Torres, L., Kaur, G., Melbourne, L. A. & Pancost, R. D. Selective chemical degradation of silica sinters of the Taupo Volcanic Zone (New Zealand). Implications for early Earth and Astrobiology. *Geobiology* **17**, 449–464 (2019).
22. Phoenix, V. R., Renaut, R. W., Jones, B. & Ferris, F. G. Bacterial S-layer preservation and rare arsenic–antimony–sulphide bioimmobilization in siliceous sediments from Champagne Pool hot spring, Waiotapu, New Zealand. *J. Geol. Soc.* **162**, 323–331 (2005).
23. Macur, R. E., Langner, H. W., Kocar, B. D. & Inskeep, W. P. Linking geochemical processes with microbial community analysis: successional dynamics in an arsenic-rich, acid-sulphate-chloride geothermal spring. *Geobiology* **2**, 163–177 (2004).
24. Connon, S. A., Koski, A. K., Neal, A. L., Wood, S. A. & Magnuson, T. S. Ecophysiology and geochemistry of microbial arsenic oxidation within a high arsenic, circumneutral hot spring system of the Alvord Desert. *FEMS Microbiol. Ecol.* **64**, 117–128 (2008).
25. Engel, A. S., Johnson, L. R. & Porter, M. L. Arsenite oxidase gene diversity among Chloroflexi and Proteobacteria from El Tatio Geyser Field, Chile. *FEMS Microbiol. Ecol.* **83**, 745–756 (2013).
26. McKenzie, E. J., Brown, K. L., Cady, S. L. & Campbell, K. A. Trace metal chemistry and silicification of microorganisms in geothermal sinter, Taupo Volcanic Zone, New Zealand. *Geothermics* **30**, 483–502 (2001).
27. Campbell, K. A. et al. The Miocene Atastra Creek sinter (Bodie Hills volcanic field, California and Nevada): 4D evolution of a geomorphically intact siliceous hot spring deposit. *J. Volcanol. Geotherm. Res.* **370**, 65–81 (2019).
28. Hamilton, A. R., Campbell, K. A. & Guido, D. M. Fossilised geothermal surface features of the Whitianga Volcanic Centre (Miocene), Coromandel Volcanic Zone, New Zealand: controls and characteristics. *J. Volcanol. Geotherm. Res.* **381**, 209–226 (2019).
29. Baumgartner, R. J. et al. Accumulation of transition metals and metalloids in sulfidized stromatolites of the 3.48 billion-year-old Dresser Formation, Pilbara Craton. *Precambrian Res.* **337**, 105534 (2019).
30. Baumgartner, R. J. et al. Pyritic stromatolites from the Paleoarchean Dresser Formation, Pilbara Craton: resolving biogenicity and hydrothermally influenced ecosystem dynamics. *Geobiology*, **22**, e12610 (2024).
31. Cady, S. L., & Farmer, J. D. In *Evolution of Hydrothermal Ecosystems on Earth (and Mars?)* (eds Brock, G. R. & Goofe, J. A.) pp. 273–299 (Wiley, 1996).
32. Nersezova, E. et al. Trace metal and organic biosignatures in digitate stromatolites from terrestrial siliceous hot spring deposits: implications for the exploration of Martian life. *Chem. Geol.* **661**, 122194 (2024).
33. Nicolau, C., Reich, M. & Lynne, B. Physico-chemical and environmental controls on siliceous sinter formation at the high-altitude El Tatio geothermal field, Chile. *J. Volcanol. Geotherm. Res.* **282**, 60–76 (2014).

34. Slagter, S. et al. Environmental controls on silica sinter precipitation revealed by radiocarbon dating. *Geology* **47**, 330–334 (2019).
35. Wilmeth, D. et al. Depositional evolution of an extinct sinter mound from source to outflow, El Tatio, Chile. *Sediment. Geol.* **406**, 105726 (2020).
36. Gong, J. et al. Morphogenesis of digitate structures in hot spring silica sinters of the El Tatio geothermal field, Chile. *Geobiology* **20**, 137–155 (2021).
37. Fernandez-Turiel, J. L., Garcia-Valles, M., Gimeno-Torrente, D., Saavedra-Alonso, J. & Martinez-Manent, S. The hot spring and geyser sinters of El Tatio, Northern Chile. *Sediment. Geol.* **180**, 125–147 (2005).
38. Guido, D. M. & Campbell, K. A. A large and complete Jurassic geothermal field at Claudia, Deseado Massif, Santa Cruz, Argentina. *J. Volcanol. Geotherm. Res.* **275**, 61–70 (2014).
39. Campbell, K. A. et al. Geyserite in hot-spring siliceous sinter: window on Earth's hottest terrestrial paleoenvironment and its extreme life. *Earth Sci. Rev.* **148**, 44–64 (2015).
40. Guido, D. M. & Campbell, K. A. Life is everywhere in sinters: examples from Jurassic hot-spring environments of Argentine Patagonia. *Geol. Mag.* **156**, 1631–1638 (2019).
41. Glennon, J. A. & Pfaff, R. M. The extraordinary thermal activity of El Tatio Geyser Field, Antofagasta Region, Chile. *GOSA Trans.* **8**, 31–78 (2003).
42. Vermaas, W. F. et al. In vivo hyperspectral confocal fluorescence imaging to determine pigment localization and distribution in cyanobacterial cells. *Proc. Natl. Acad. Sci.* **105**, 4050–4055 (2008).
43. Ye, J. et al. Arsenic biomethylation by photosynthetic organisms. *Trends Plant. Sci.* **17**, 155–162 (2012).
44. Saunders, J. K. et al. Complete arsenic-based respiratory cycle in the marine microbial communities of pelagic oxygen-deficient zones. *Proc. Natl. Acad. Sci. USA* **116**, 9925–9930 (2019).
45. Tice, M. M. & Lowe, D. R. The origin of carbonaceous matter in pre-3.0 Ga greenstone terrains: a review and new evidence from the 3.42 Ga Buck Reef Chert. *Earth Sci. Rev.* **46**, 259–300 (2006).
46. Westall, F. et al. Archean (3.33 Ga) microbe-sediment systems were diverse and flourished in a hydrothermal context. *Geology* **43**, 615–618 (2015).
47. Teece, B. L. et al. Exceptional molecular preservation in the late Jurassic Claudia palaeo-geothermal field (Deseado Massif, Patagonia, Argentina). *Org. Geochem.* **173**, 104504 (2022).
48. Amend, J., Saltikov, C., Lu, G.-S. & Hernandez, J. Microbial arsenic metabolism and reaction energetics. *Rev. Mineral. Geochem.* **79**, 391–433 (2014).
49. Stolz, J. F. et al. Arsenic and selenium in microbial metabolism. *Annu. Rev. Microbiol.* **60**, 107–130 (2006).
50. Iler, R. K. *Chemistry of Silica – Solubility, Polymerization, Colloid and Surface Properties and Biochemistry* (Wiley Interscience, 1979).
51. Swedlund, P. J. & Webster, J. G. Adsorption and polymerisation of silicic acid on ferrihydrite, and its effect on arsenic adsorption. *Water Res.* **33**, 3413–3422 (1999).
52. Sanchez-Garcia, L. et al. Microbial biomarker transition in high-altitude sinter mounds from El Tatio (Chile) through different stages of hydrothermal activity. *Front. Microbiol.* **9**, 3350 (2019).
53. Hoeft, S. E., Kulp, T. R., Han, S., Lanoil, B. & Oremland, R. S. Coupled arsenotrophy in a hot spring photosynthetic biofilm at Mono Lake, California. *Appl. Environ. Microbiol.* **76**, 4633–4639 (2010).
54. Van Lis, R., Nitschke, W., Duval, S. & Schoepp-Cothenet, B. Arsenics as bioenergetic substrates. *Biochim. Biophys. Acta* **1827**, 176–188 (2013).
55. Hu, W. et al. Life on the edge: microbial biomineralization in an arsenic- and lead-rich deep-sea hydrothermal vent. *Chem. Geol.* **533**, 119438 (2020).
56. Chen, S. C. et al. The Great Oxidation Event expanded the genetic repertoire of arsenic metabolism and cycling. *Proc. Natl Acad. Sci. USA* **117**, 4925–4934 (2020).
57. Djokic, T., Van Kranendonk, M. J., Campbell, K. A., Walter, M. R. & Ward, C. R. Earliest signs of life on land preserved in ca. 3.5 Ga hot spring deposits. *Nat. Commun.* **8**, 15263 (2017).
58. Ruff, S. W. & Farmer, J. D. Silica deposits on Mars with features resembling hot spring biosignatures at El Tatio in Chile. *Nat. Commun.* **7**, 1–10 (2016).
59. Guido, D. M. & Campbell, K. A. Jurassic hot spring deposits of the Deseado Massif (Patagonia, Argentina): characteristics and controls on regional distribution. *J. Volcanol. Geotherm. Res.* **203**, 35–47 (2011).
60. Cotten, J. et al. Origin of anomalous rare-earth element and yttrium enrichments in subaerially exposed basalts: evidence from French Polynesia. *Chem. Geol.* **119**, 115–138 (1995).
61. Pierce, M. L. & Moore, C. B. Adsorption of arsenite and arsenate on amorphous iron hydroxide. *Water Res.* **16**, 1247–1253 (1982).
62. Govindaraju, K. 1995 Working values with confidence limits for twenty-six CRPG, ANRT AND IWG-GIT geostandards. *Geostand. Newslett.* **19**, 1–32 (1995).
63. Henke, B., Gullikson, E., & Davis, J. X-ray interactions: photoabsorption, scattering, transmission, and reflection at $E = 50$-30,000 eV, $Z = 1$-92. *At. Data Nucl. Data Tables* **54**(2), 181–342 (1993).
64. Slagter, S. et al. Data in the manuscript entitled "Arsenic-cycling metabolism recorded in hot spring silica deposits" data set. Zenodo https://doi.org/10.5281/zenodo.20160239 (2026).
65. Ravel, B. & Newville, M. ATHENA, ARTEMIS, HEPHAESTUS: data analysis for X-ray absorption spectroscopy using IFEFFIT. *J. Synchrotron Radiat.* **12**, 537–541 (2005).
66. Walters, W. et al. Improved bacterial 16S rRNA gene (V4 and V4-5) and fungal internal transcribed spacer marker gene primers for microbial community surveys. *mSystems* **1**, e00009–e00015 (2016).
67. Dowd, S. E., Sun, Y., Wolcott, R. D., Domingo, A. & Carroll, J. A. Bacterial tag-encoded FLX amplicon pyrosequencing (bTEFAP) for microbiome studies: bacterial diversity in the ileum of newly weaned Salmonella-infected pigs. *Foodborne Pathog. Dis.* **5**, 459–472 (2008).
68. Caporaso, J. G. et al. QIIME allows analysis of high-throughput community sequencing data. *Nat. Methods* **7**, 335–336 (2010).
69. DeSantis, T. Z. et al. Green genes, a Chimera-checked 16S rRNA gene database and workbench compatible with ARB. *Appl. Environ. Microbiol.* **72**, 5069–5072 (2006).

Acknowledgments

The authors sincerely thank the beamline support from Dr(s). Matt Newville and Tony Lanzirotti.

Author contributions

S.S., K.M., M.v.Z., S.V.L., T.C., and D.G. performed the fieldwork. S.S., K.M., and B.M. carried out synchrotron-based analyses. S.S. and K.M. performed SEM analyses. G.A. and S.V.L. performed the CLSM and major- and trace-element analyses.

Funding

This project has received funding from the European Research Council (ERC) under the European Union's Horizon 2020 research and innovation programme (grant agreement no. 646894) to M.v.Z. and the Agencia Nacional de Promocón Científica y Tecnológica (PICT 2014-1704 project) to D.M.G. M.v.Z. discloses that support for this work was provided by the IPGP multidisciplinary program PARI and by the Région Ile-de-France SESAME grant no. 12015908.

Competing interests

The authors declare no competing interests.

Additional information

Supplementary information The online version contains supplementary material available at https://doi.org/10.1038/s43247-026-03672-z.

Correspondence and requests for materials should be addressed to Silvina Slagter.

Peer review information *Communications Earth* and Environment thanks Kelsey R. Moore, David Madrigal-Trejo and the other, anonymous, reviewer(s) for their contribution to the peer review of this work. Primary Handling Editors: Mojtaba Fakhraee, Alice Drinkwater, and Mengjie Wang. A peer review file is available.